We are IntechOpen,
the world's leading publisher of
Open Access books
Built by scientists, for scientists

6,900
Open access books available

186,000
International authors and editors

200M
Downloads

154
Countries delivered to

Our authors are among the

TOP 1%
most cited scientists

12.2%
Contributors from top 500 universities

CLARIVATE ANALYTICS
BOOK CITATION INDEX
INDEXED

WEB OF SCIENCE™

Selection of our books indexed in the Book Citation Index
in Web of Science™ Core Collection (BKCI)

Interested in publishing with us?
Contact book.department@intechopen.com

Numbers displayed above are based on latest data collected.
For more information visit www.intechopen.com

Hydrodynamic Effects of Sedimentation on Mass Transport Properties in Dead Water Zone of Natural Rivers

Michio Sanjou

Department of Civil and Earth Resources Engineering, Kyoto University
Japan

1. Introduction

We can often see dead water zones composed of consecutive groynes in natural rivers. The groynes are generally constructed in the bank of actual rivers in order to navigate stream direction and to prevent bank erosion. Dead water zones such as side cavities are also observed in harbors of rivers, and it is well known that there are significant differences between streamwise velocities of the mainstream and the cavity zone. Of particular significance is that shear instability related to the velocity difference induces coherent horizontal vortex along the boundary of the mainstream and the cavity. Further, large-scale gyres are formed in the dead water zone which conveys suspended sediment from the main-channel, and local sedimentations are promoted in the cavity as shown in photo 1. So, it is necessary to reveal the hydrodynamic properties included with turbulence phenomena in order to control sedimentation reasonably. Akkerman et al.(2004) conducted the sensitivity analysis with a 1-dimensional morphodynamic model, and they discussed the several effects on sedimentation and flood water depth after the occurrence of groyne damage. Recently, permeable groynes are proposed to realize stable bed condition. For example, Kadota & Suzuki (2010) discussed experimentally effects of the permeability and the scales of the groynes and stone gabion in submerged and emerged flow conditions. Tominaga & Sakaki (2010) conducted ADV measurements around the permeable groynes in a natural river, and they evaluated distributions of bed shear stress accurately.

In these cavities, not only sedimentation but also congestion of pollutants is often highlighted. It is thus very important to investigate mass & momentum exchanges between the main-channel and the side-cavity in river environment and hydraulic engineering. The above-mentioned horizontal gyres and coherent turbulent structures play significant roles on mass and momentum exchanges. Uijttewaal et al.(2001) measured distribution of dye concentration and pointed out that aspect ratio of side cavity has significant effects on exchange rate of mass between the mainstream and the dead water zone. Weitbrecht et al.(2007) have also conducted laboratory measurements, in which distribution of velocity components and dye were obtained. They examined the relation between the exchange rate and the bed configuration of the cavity.

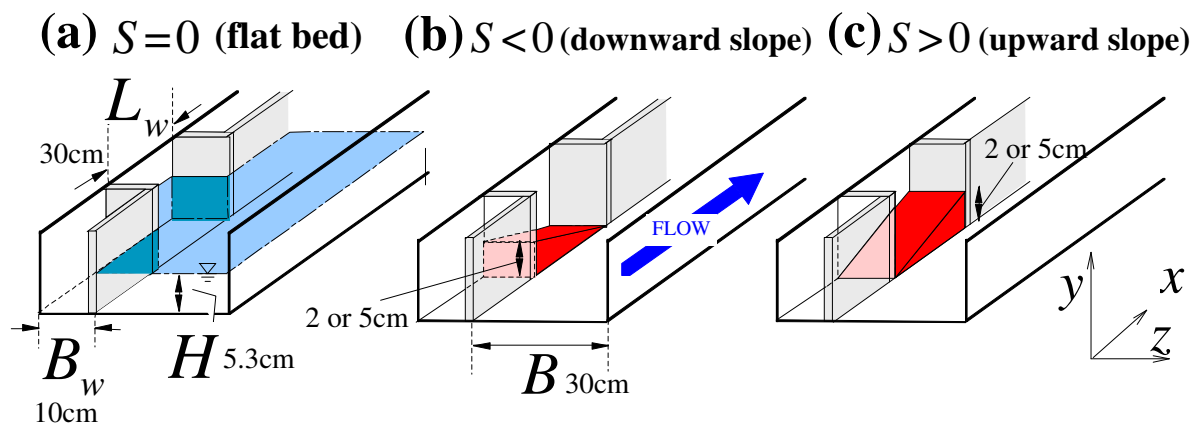Photo 1. Sedimentation in cavity zone of natural river (Yada river in Nagoya, Japan)

Fig. 1. Bed configurations in the present experiments

U_m (cm/s)	H (cm)	B (cm)	B_w (cm)	L_w (cm/s)	Fr	Re	S
							-1/6
							-1/15
12	5.3	30	10	30	0.17	6360	0
							1/15
							1/6

Table 1. Hydraulic condition

However, there remain uncertainties about accurate evaluations of exchange velocity, effects of the bed formation on mass transport and physical modeling of mass exchange in the side-cavity flows. Therefore, in this study, PIV and LIF were conducted in a laboratory flume using a laser light sheet and high-speed CMOS camera in order to reveal hydrodynamic characteristics and turbulence structure and evaluate exchange properties of dye concentration across the junction.

2. Experimental procedure

2.1 Hydrodynamic condition and bed configuration

The experiments were conducted in a 10m long, 40cm width glass-made tilting flume. The coordinate was chosen that (x, y, z) correspond to the streamwise, vertical and spanwise directions, respectively. The channel bed was chosen as the vertical origin ($y=0$). In the measurement section, 7m downstream from the channel entrance, a side-cavity is placed by acrylic plates. The widths of the main-channel and the cavity are $B=30$cm and $B_w=10$cm，respectively. The streamwise lenght of the cavity is $L_w=30$cm. Table 1 shows hydraulic condition, in which the water depth is $H=5.3$cm, the bulk-mean velocity is $U_m=12$cm/s, Froude number is $Fr=0.166$ and Reynolds number is $Re=6360$. We chosen several kinds of bed configurations in the cavity as shown in Fig.1. S is a parameter to indicate the bed configuration. Negative sign of S means downward incline as shown in Fig.1 (b), and positive one means upward incline as shown in Fig.1 (c). $S=0$ means the flat bed condition. The absolute value of S means the inclination of the bed. In the present study, the elevation gaps are 2cm and 5cm for the mild and steep conditions, respectively.

2.2 Measurement method

The 2mm thick laser light sheet (LLS) was generated by 3W Ar-ion laser using a cylindrical lens. The illuminated flow images were taken by a CMOS camera (1000×1000pixels) with 100Hz frame-rate and 30Hz sampling-rate. The sampling duration is 60 seconds for each case. The instantaneous velocity components ($\tilde{u}$, $\tilde{w}$) on the horizontal plane were calculated by the PIV algorithm. Further, in the non-flat conditions, LLS was also projected along the bed slope. This is called as "inclined LLS measurements". In the "horizontal-LLS measurements", the elevations of the LLS were $y=1$cm, 2cm, 2.5cm, 5cm for the all cases. The "inclined LLS measurements" were carried out for the steep slope conditions, in which the gap of the LLS and the bed surface is 1cm.

The distribution of dye concentration is measured by the LIF method, in which the sharp-cut filter was put on the lens of the CMOS camera in order to obtain clear concentration image illuminated by the LLS. The instantaneous distribution of the dye concentration C was calculated by using brightness values of these LIF images. The Dye (Rhodamine-B), the concentration of which is 0.2mg/l, was dissolved in the cavity. At the initial stage of the measurements, the cavity and the main-channel are separated by the plate. After remove of the plate, the dye exchange and transfer motions were captured by the CMOS camera. Borg et al. (2001) pointed out that there exists a linear relation between image brightness and dye concentration under the small concentration conditon($C<0.2$mg/l). This fact was surely recognized in this study by using the present data, and a linear calibration curve was obtained.

3. Currents and turbulence structure

In the present section, the results of velocity measurements using PIV techniques are introduced. Time-averaged velocity distribution, turbulence properties and the coherent structure are examined. Further, the influences of the bed configurations on the hydrodynamic characteristics are also considered.
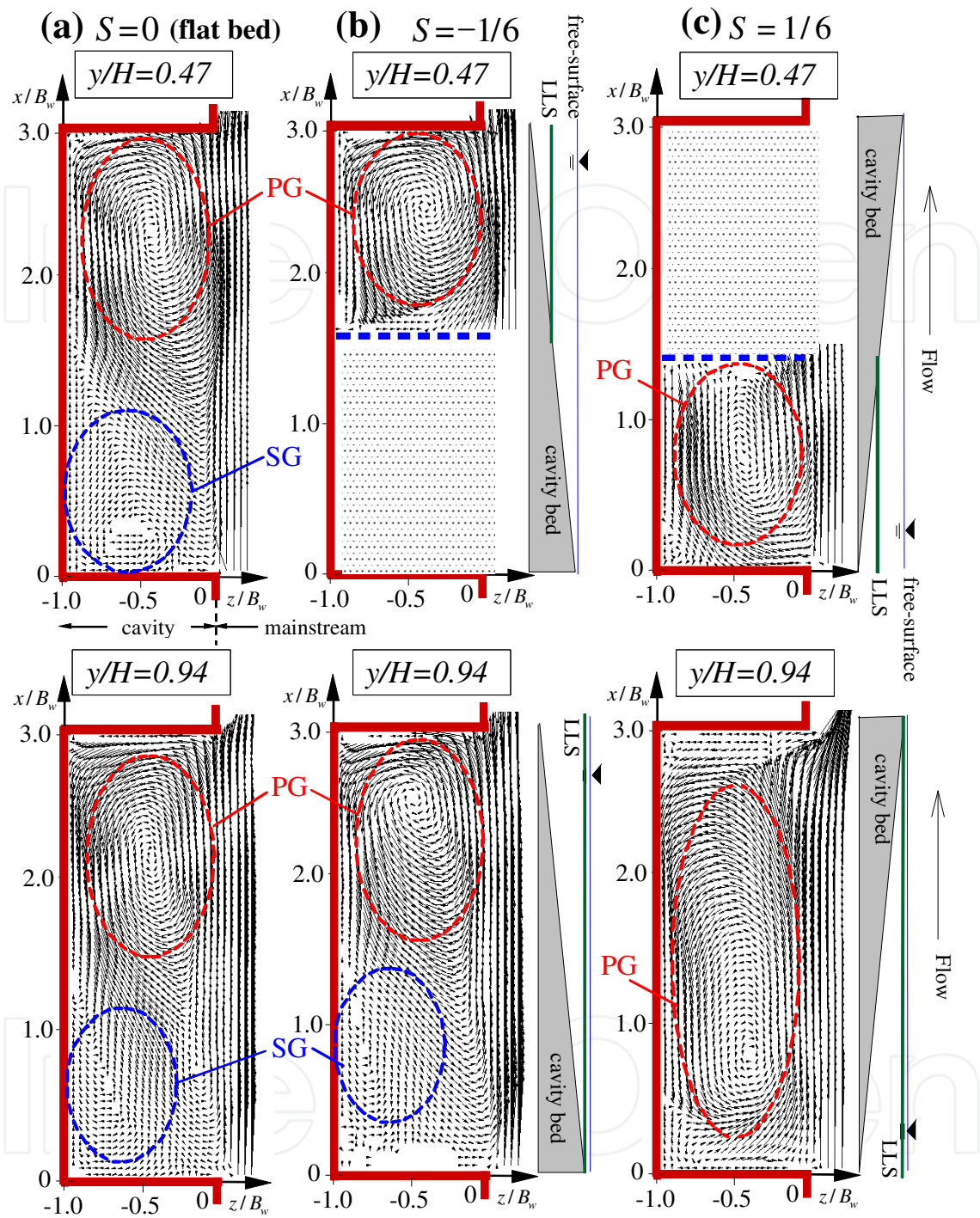
Fig. 2. Time-averaged horizontal velocity vectors

3.1 Time-averaged horizontal velocity components

Fig.2 shows time-averaged horizontal velocity vectors (U,W) at y/H=0.47 and 0.94. At the near free-surface, y/H=0.94, two kinds of large scale gyres with counter rotations are observed in the S =0 and –1/6. Whereas, single gyre structure appears and it covers a whole region of the canopy in the S =1/6. The PG is a horizontal circulation induced by the main-stream, and it was observed, irrespective of the elevation and the geometry of the canopy

bed. The secondary gyre (SG) seems to be generated by the MG. In the S =1/6, the contact area between the main stream and the cavity zone decreases downstream, and the inflow from the mainstream toward the side canopy becomes smaller compared with those observed in the S =0 and –1/6. Thus, the position of PG is shifted toward upstream-side of the side canopy, and the sufficient space could be not kept to generate SG in the S =1/6. At the mid-depth layer, y/H=0.47, the PG and the SG are observed in the same manner as those of y/H=0.94 in the flat condition. In contrast the only PG is formed in the mid depth layer in the non-flat conditions.

3.2 Scale evaluations of horizontal gyres

Figs. 3 and 4 show the distributions of vorticity with vertical axis, $\Omega \equiv \partial U / \partial z - \partial W / \partial x$ and delta value Δ at y/H=0.94, for S =-1/6, 0 and 1/6, respectively.

Chong and Perry (1990) considered the Eigenvalue σ of the velocity shear tensor ($\partial \tilde{u}_i/\partial x_i$) in shear layers. The Eigenvalue equation of 2D shear flow is given by

$$\sigma^2 - P\sigma + Q = 0 \tag{1}$$

in which

$$P \equiv \frac{\partial \tilde{u}_i}{\partial x_i} = 0 \quad \text{and} \quad Q \equiv \frac{1}{2}\left(\left(\frac{\partial \tilde{u}_i}{\partial x_i} \right)^2 - \frac{\partial \tilde{u}_i}{\partial x_i} \frac{\partial \tilde{u}_j}{\partial x_j} \right) \tag{2}$$
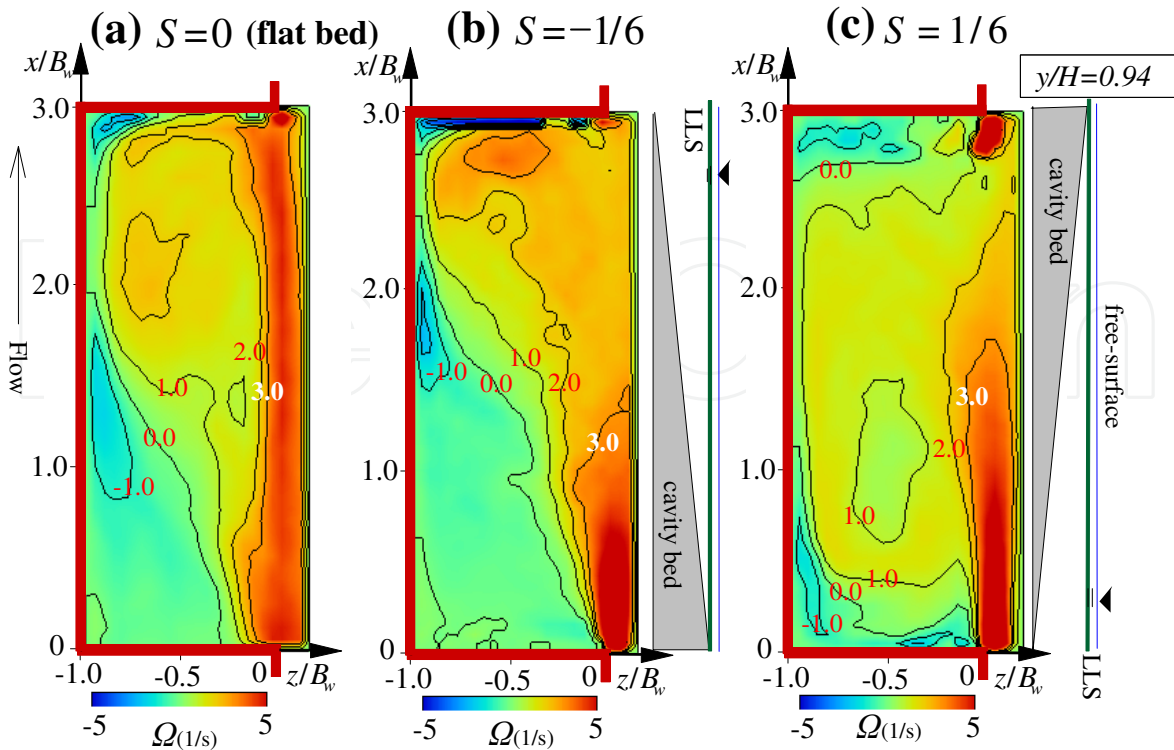
$$\Delta \equiv P^2 - 4Q \tag{3}$$

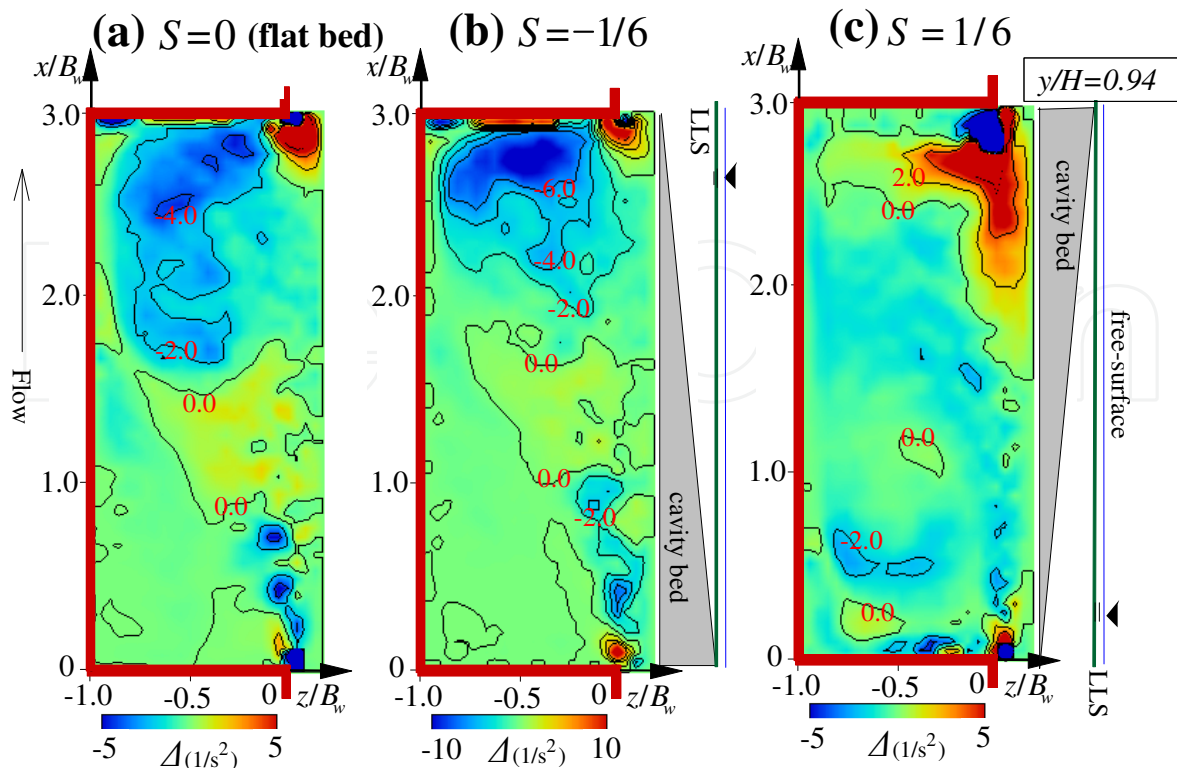Fig. 3. Distributions of time-averaged vorticity with vertical axis

Fig. 4. Horizontal distributions of delta-value

where $\tilde{u}_i$=instantaneous velocity components with i=1 and 2 herein. Complex Eigenvalues occur if the discriminant Δ is negative. Chong and Perry assumed that $\Delta<0$ corresponds to the existence of a vortex core, and verified the validity of such a vortex detection, referred to as the *delta method* in shear layers.

Positive and negative values of the vorticity mean anti-clockwise and clockwise rotations, respectively. It should be noticed that even if the fluid does not rotate, large vorticity appears in the shear layer, where spatial gradient of the velocity components is dominant. Therefore, in the present study, not only the vorticity but also the delta value is used to detect gyre regions and to measure the corresponding areas.

In the flat bed condition (S=0), positive distribution of Ω is observed along the junction, in which streamwise velocity shear $\partial U / \partial z$ is very large and furthermore small-scale shedding vortices are generated periodically by the shear instability. It is noted that the positive and negative regions appears corresponding to the PG and SG as shown in Fig.2. It is found that the delta value becomes negative in these regions.

In S=-1/6, the distributions of the vorticity and delta seem to be similar to those of the flat condition. The positive voriticity region corresponding to the PG shifts toward the downstream-side compared with the flat condition. This property is also observed in the distribution of the delta. This is because the PG is transported toward the downstream-side in the cavity due to the effect of the bed configuration.

In contrast, in S=1/6, the positive vorticity and the negative delta are dominant in the cavity. These properties correspond well with the horizontal distributions of velocity vectors as shown in Fig.2. In the upstream side of the cavity, the negative vorticity and the negative delta appear corresponding to the SG which becomes very small due to the bed configuration effect.
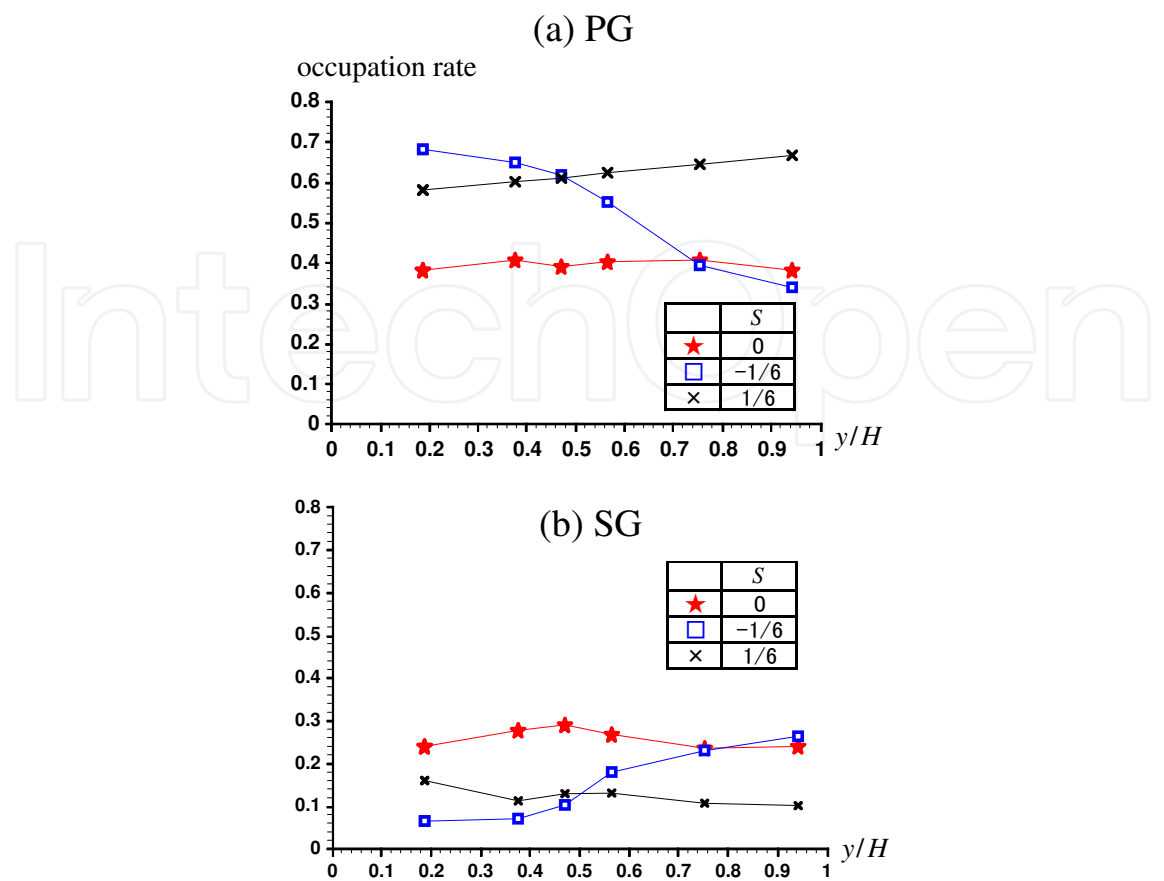
Fig. 5. Area occupation rates of primary gyre and secondary gyre in the cavity
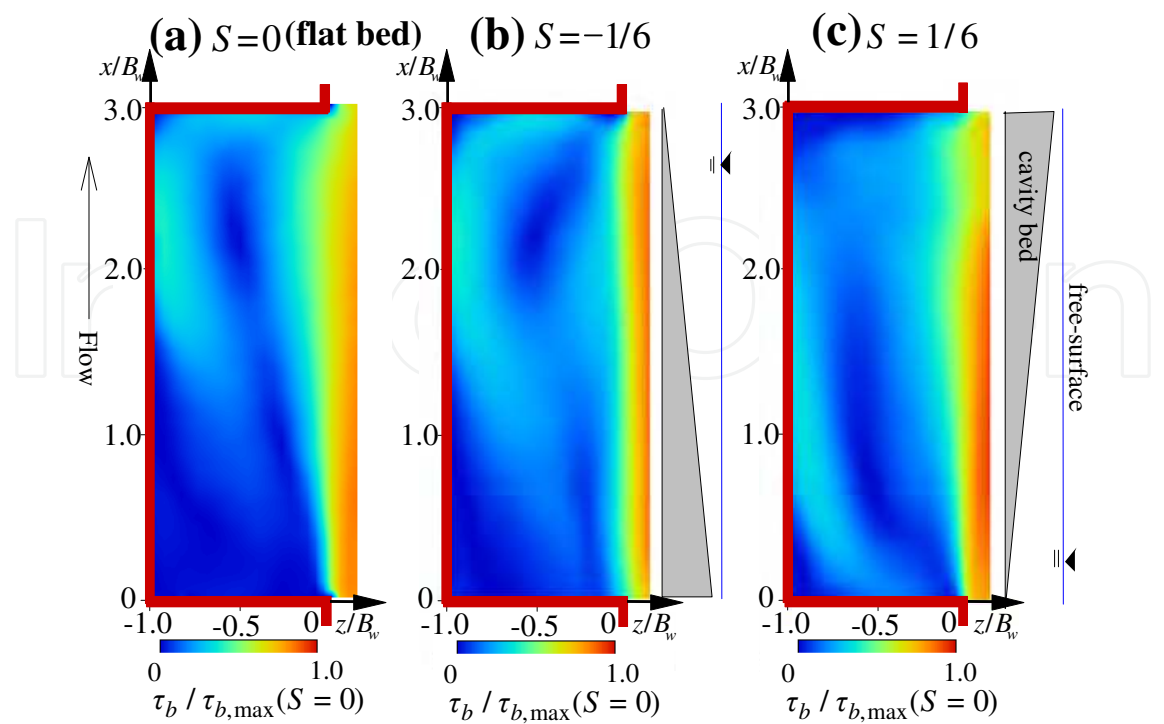

Fig. 6. Distributions of bed shear stress in the cavity

The total area of the PG was calculated by summing the local square, in which the positive vorticity and negative delta appear. In the same way, the total area of SG was calculated by the local square, where negative vorticity and negative delta exist. Fig.5 (a) and (b) show areas of PG and SG normalized by a total cavity area. In the S =0 and -1/6, the area of PG is comparable with that of SG near the free surface. In contrast, in the S =1/6, the area of PG is larger and that of SG is smaller than those observed in S =0, -1/6.

3.3 Distribution of bed shear stress

Figs. 6 shows the distributions of bed shear stress τ_b in the cavity. τ_b was calculated by using the viscosity μ and the velocity gradient, i.e., $\mu \partial \sqrt{U^2 + W^2} / \partial y$. For the slope conditions, The LLS was projected pararell to the cavity bed with the 1cm gap between them, and thus, the near-bed velocities parallel to the bed surface (U, W) could be obtained by the PIV. It is found that small bed shear stress zones are observed in the core of the PG. They also appear in the SG region. In S =1/6, the small bed shear stress zone relevant to the PG is shifted toward the upstream-side compared with S =0 and 5. It should be noticed that local sedimentations are promoted significantly in these low-speed regions. In contrast, it is expected that a scour process is observed in the outer side of PG. The present results allow us to understand that the formations of PG and SG play significant roles on the sedimentation in the cavity.
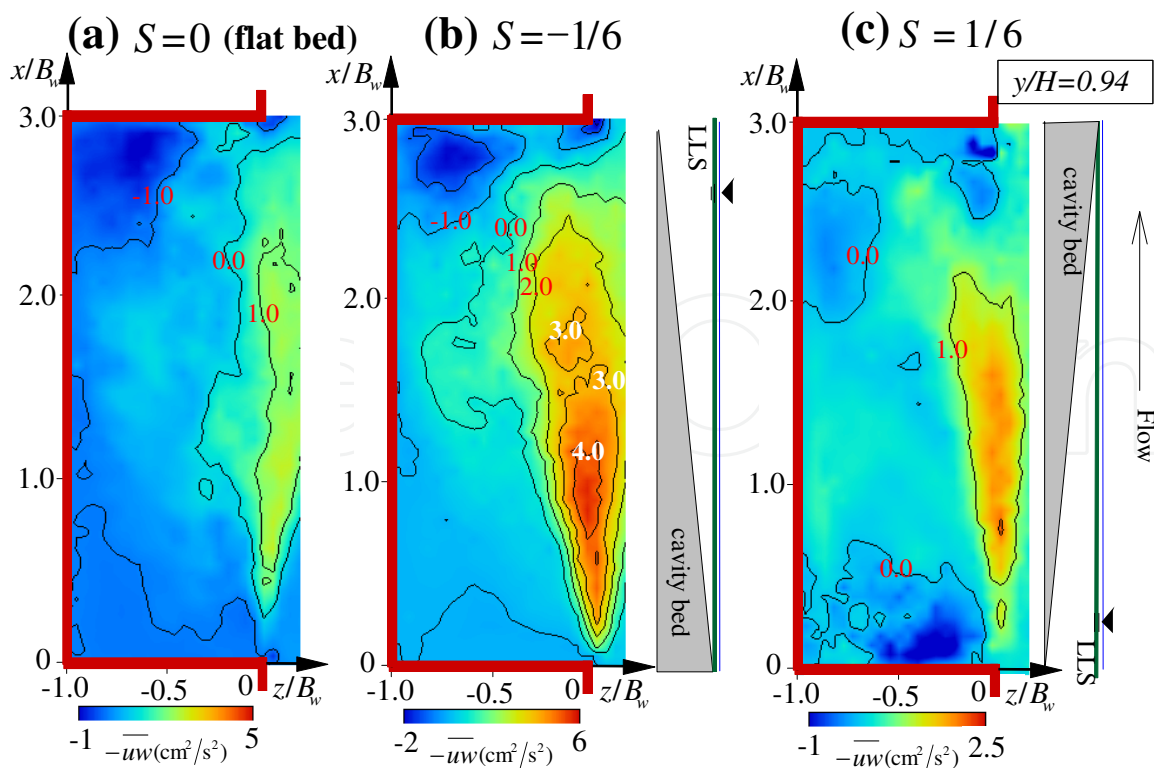
Fig. 7. Horizontal distributions of Reynolds stress

3.4 Distribution of Reynolds stress

Fig.7 shows horizontal distributions of Reynolds stress $-\overline{uw}$ at y/H=0.94. The large and positive Reynolds stress zone is formed along the junction between the mainstream and the cavity. The shear instability induces such a strong turbulence layer irrespectively of the bed configuration. It is found that Reynolds stress becomes largest in the downward slope condition, S =-1/6. The spanwise currents from the cavity toward the mainstream appear the upstream-side of the PG in Fig.2. They are accelerated more nearer the upstream-side of the cavity, where the water depth decreases due to the bed configuration. Thus, larger Reynolds stress may be generated much more in the down slope condition than other bed configurations.

Fig.7 shows spatial variation of Reynolds stress in the junction. A peak Reynolds stress appears at x/B_w =1.0 in the down slope condition, S =-1/6. In contrast, all most constant value is observed except the upstream and downstream walls in the cavity. The Reynolds stress of the downward slope condition (S =-1/6) is twice as large as those of the flat (S =0) and the upward slope conditions (S =1/6), in which same order Reynolds stress is observed.

3.5 Instantaneous velocity properties

Fig. 9 shows time-series of the distributions of instantaneous Reynolds stress $-uw$ and discriptions of horizontal velocity components $(\tilde{u},\tilde{w})$ every 1s for S =0. The elevation is y/H=0.94. At t=0s, the circle A indicates the coherent structure of fluid percel which is transported strongly toward the mainstream. This is called as sweep motion in the present study. The shedding vortex follows the sweep as indicated by the circle B, in which the fluid percel intrudes into the cavity accompanied with the strong positive Reynolds stress. This is called as ejection. These coherent motions are convected downstream at t=1s, and in contrast, the sedding vortex in the circle B is disappearing. A new sweep motion appear as indicated by the circle C. At t= 2s, it is found that a large amont of fluid is transported toward the cavity zone by the sweep (B). Furhter, a shedding vortex (D) is generated together with positve Reynolds stress. This result suggetst that mass transfer process between the mainstream and the cavity is promoted significantly by such coherent strucures.

Figs. 10 (a) and (b) show examples of the instantanesous velocity fields for S =-1/6 and 1/6. In S =-1/6, the sedding vortex is observed as indicated by the circle A, and the sweep motion (B) is formed. The sweep seem to be larger than that obserbed in S =0. It is found that the PG is also visualized even in the instantaneous velocity field. In S =1/6, the ejection is observed as indicated by circle A. However, the sedding vortex is not be regonnized. This result correspond well to the finding that Reynolds stress is smaller in the S =1/6 than the S =0 and –1/6 as shown in Fig.7. It is therefore found that the bed configuration has striking impacts on turbulence production in the cavity.

Therefore, horizontal and vertical LLSs are projected simultaneously, and these illuminated planes are taken by dual CMOS cameras. Fig.11 shows examples of time series of instantaneous velocity vectors in the horizontal and vertical planes every 0.6 seconds. The

positions of these planes are y/H=0.94. (near free-surface) and z/B=-0.2 (near the junction between the main-channel and the cavity). The white broken line of horizontal views and the red one of vertical views indicate the positions of vertical and horizontal illuminated planes, respectively. The contours mean distributions of instantaneous Reynolds stress $-uw$ and vertical velcotiy $\tilde{v}$ for the horizontal and vertical views, respectively.

In the S =0, red circle indicates large Reynolds stress observed at the junction near the upstream side of the cavity. It is inferred that shedding vortex produces locally the large Reynolds stress distribution. Further, the Reynolds stress seems to intrude toward the cavity. It is found by comparison of the horizontal and vertical views that upward currents appear in the intruding region of large Reynolds stress. The downward current follows the upward one, and it is thus suggested that strong 3-D structure is formed near the junction, when shedding vortex enter to the cavity. In the S =-1/6, a similar 3-D structure is observed in the same manner as one of S =0. Particularly, after the transfer of Reynolds stress toward the cavity, it is accompanied with downward current in the downstream side of the cavity. In the S =1/6, upward currents are dominant in the whole area of the vertical plane. Of particular significance is that larger upward flows are generated than the surrounding positions at the inrushing time of sweep motion.
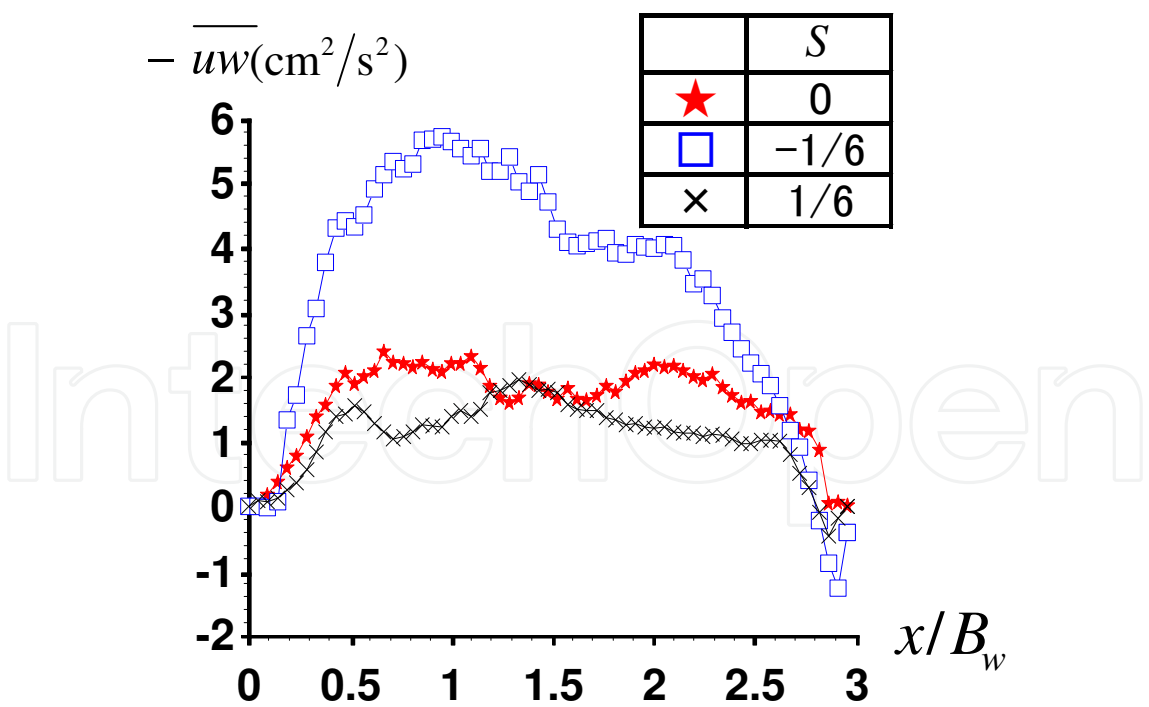

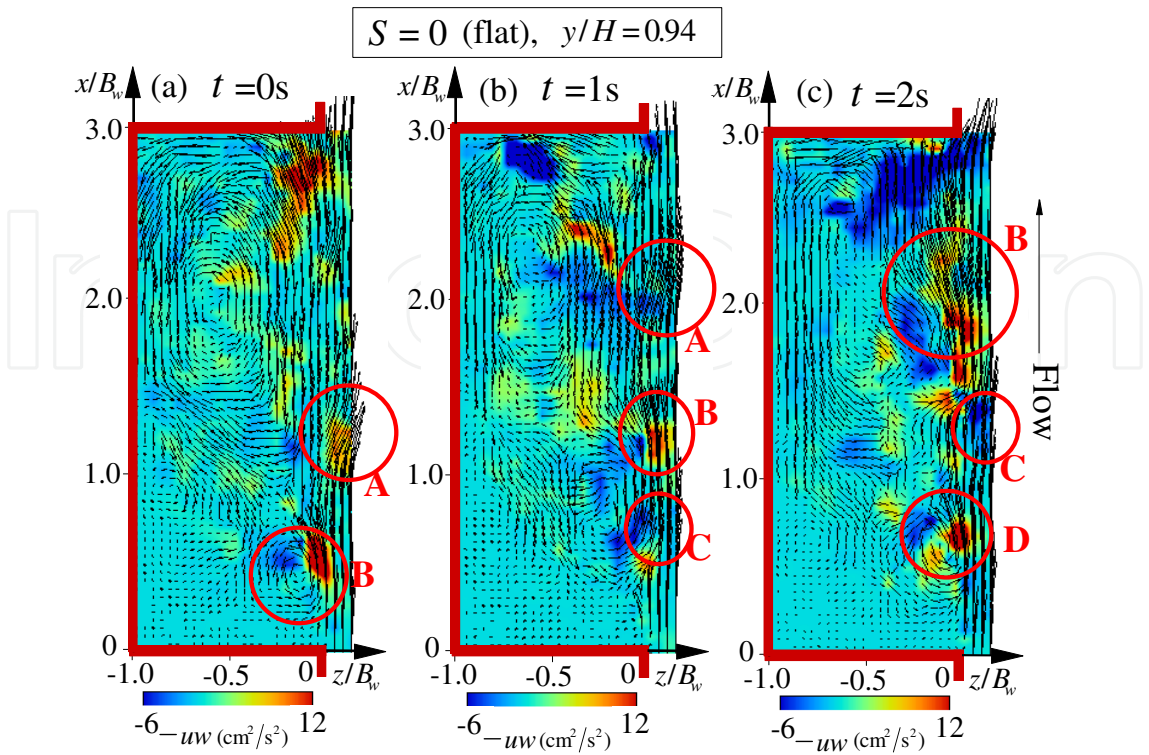Fig. 8. Comparison of Reynolds stress profiles among different bed configurations

Fig. 9. Time-series of the distributions of instantaneous Reynolds stress and horizontal velocity components for the flat bed configuration
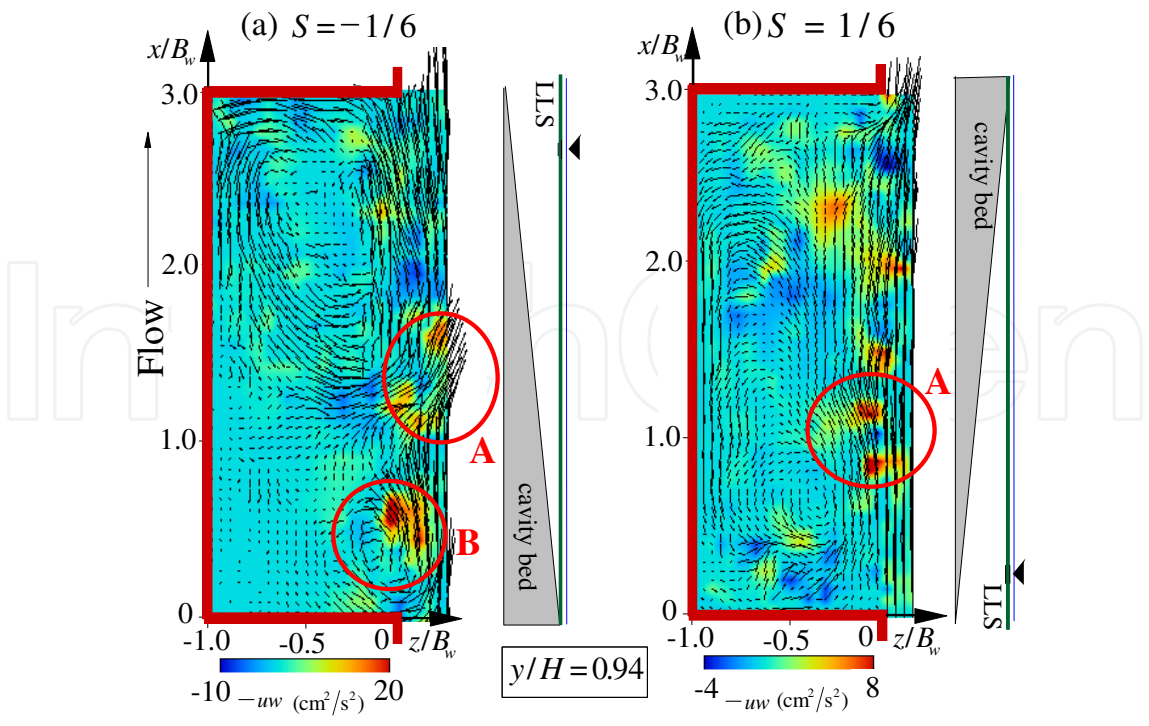

Fig. 10. Distributions of instantaneous Reynolds stress and horizontal velocity components for the slope bed configurations
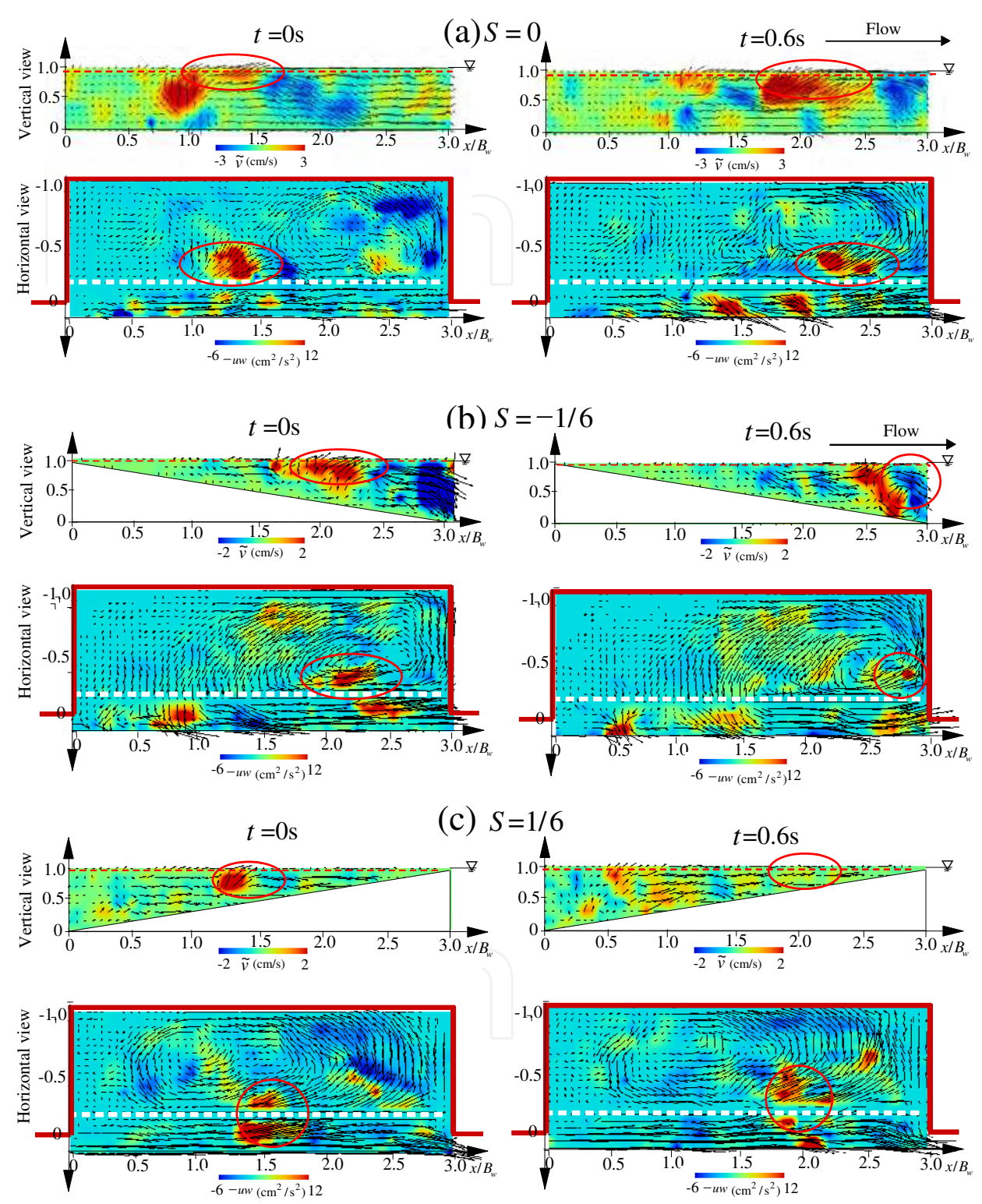
Fig. 11. Instantaneous velocity vectors in the horizontal and vertical planes

In Figs.9 and 10, only horizontal currents are focused, and thus, there remain many uncertainties about vertical component of velocity. Particularly, it is very significant to reveal how horizontal vortices and gyres induces upward and downward flows.
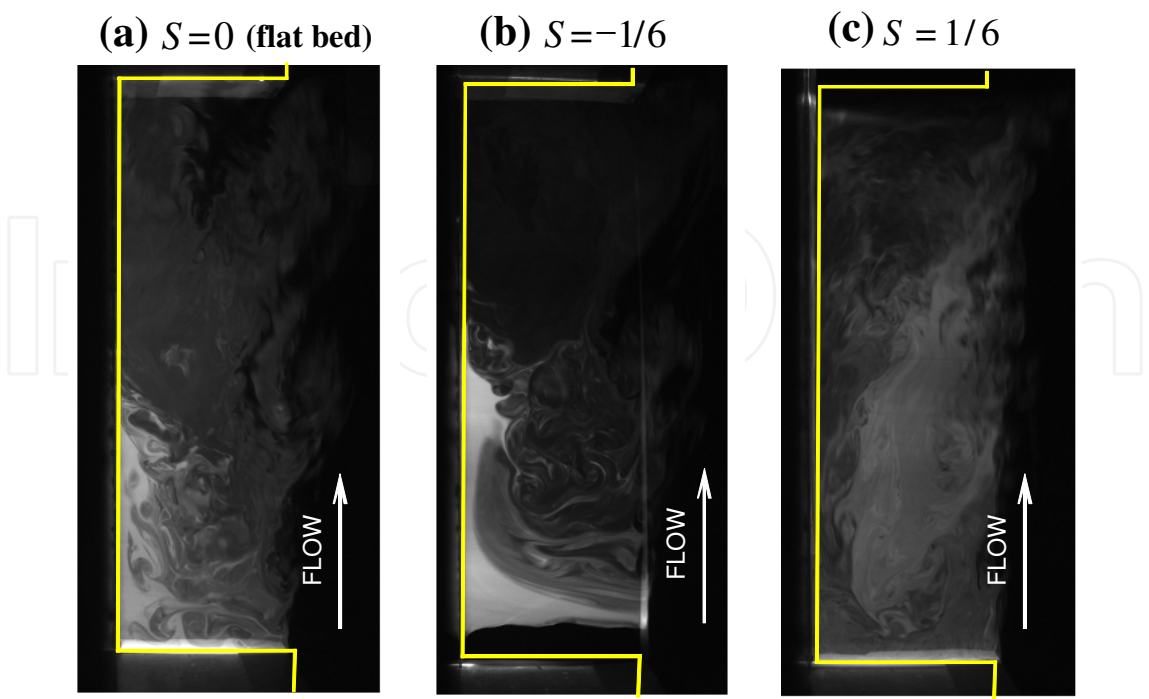
Fig. 12. Dye transport in different types of bed conditions

4. Mass transfer properties between mainstream and cavity

The coherent turbulent structures such as shedding vortex, sweep and ejection play significant roles on mass and sediment transfers. However, there are many uncertainties about relation between the turbulence and mass transfers. In this section, exchange properties of dye concentration and effects of sedimentation on them are considered.
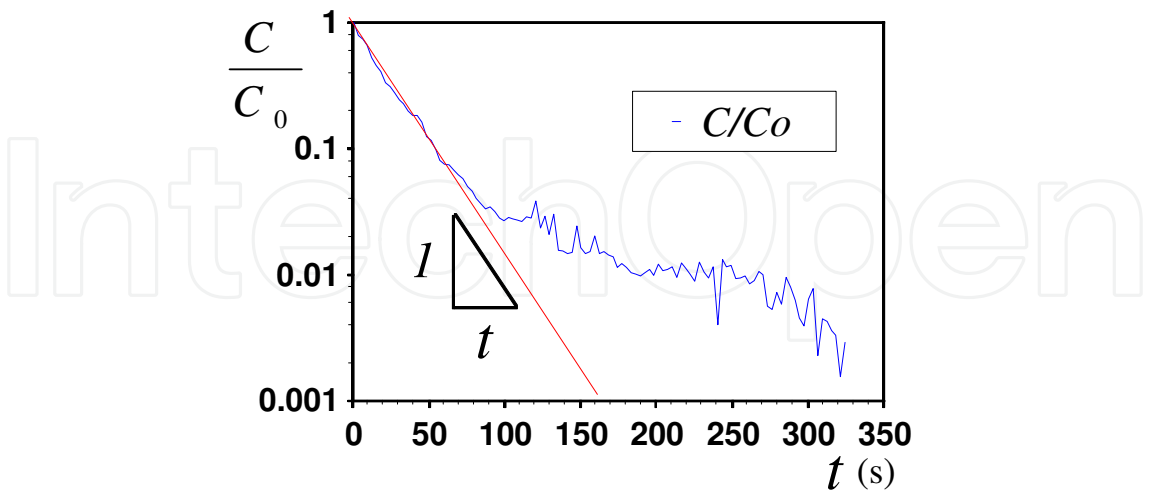

Fig. 13. Time-variation of dye concentration for the flat condition$_o$

4.1 Dye visualization of mass transfer

Fig.12 shows instantaneous distribution of dye concentration at y/H=0.94. The mass exchange is promoted significantly in the PG region, and, in contrast, the dye is

accumulated in the SG region for S =0 and -1/6. These results coincide well with those of previous experiments conducted by Uijttewaal et al and Weitbrecht et al. Whereas, for the S =1/6, although horizontal area of PG covers the almost whole cavity zone, circulation velocities may comparatively weak, and dye remains in the PG region. Of particular significance is that mass transport in the side cavity depends strongly on the formation properties of the horizontal gyres.

4.2 Evaluation of transfer coefficient

Transport equation for concentration exchange between the mainstream and the dead water zone such as side cavity, is follows as;

$$DC/Dt=(kU_m/B_w)(C-C_0) \tag{4}$$

C is instantaneous concentration, C_0 is initial concentration value and k is transfer coefficient given by following equation.

$$k=B_m/(UT) \tag{5}$$

T is the specific time when C/C_0 becomes 1/10. It is calculated by using time-variation of C during linearly decrease stage.

Fig.13 shows time-series of concentration at y/H=0.94. for the flat-bed condition. The concentaration decreases linearly from t=0s to 50s, and thereafter, time-variation becomes smaller. As pointed out by Uijttewaal et al, the linear-decrease corresponds to the mass exchange promoted by the PG, and incontrast, after the contribution of the PG, the time-variation becomes small due to stagnating induced by the SG. This suggests that the PG plays significant rolls on the mass transfer beneath interface between the main-channel and the dead water zone. Therefore, the transfer coefficient k was evaluated by applying the time-gradient of concentration to Eqs.(4) and (5).
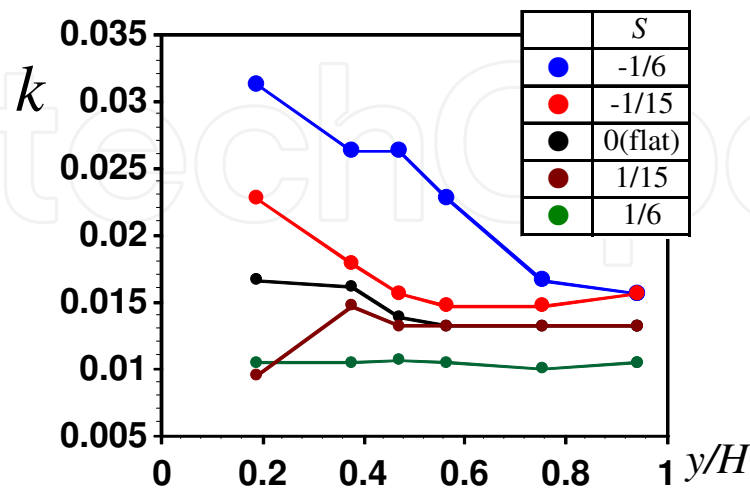

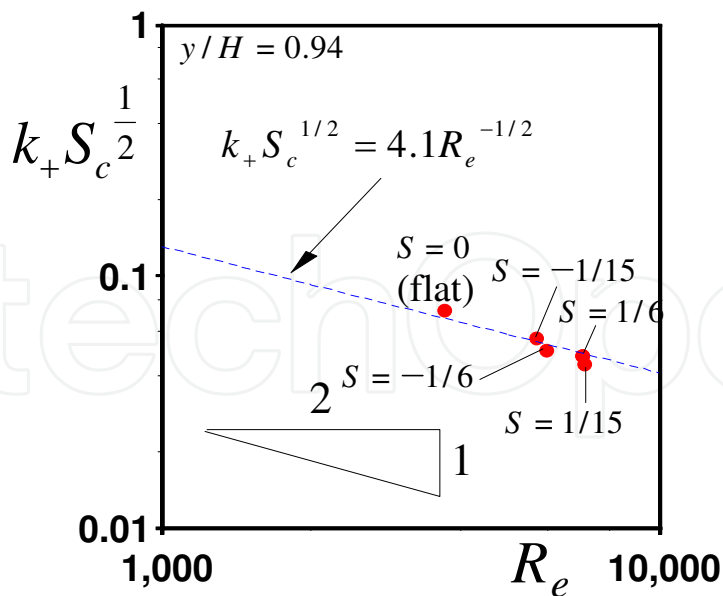Fig. 14. Vertical profile of transfer coefficient

Fig. 15. Relation between transfer velocity and Reynolds number

Fig.14 shows vertical profile of transfer coefficient. It decreases toward the free-surface in the $S < 0$ series, and this is because area of the SG, in which mass is accumulated as mentioned above, becomes larger nearer the free-surface. In the flat bed case, the structures of the PG and SG are almost constant in the vertical direction, and vertical variation of k is comparatively small. In the $S > 0$ series, the single gyre is formed in the whole depth region, and dye concentration is captured in the PG region without transfer to the main stream. It is thus found that variations of k are smaller than those observed in the $S = 0$ and $S < 0$.

4.3 Parameterization

In the studies on gas transfer phenomena, reasonable parameterizations are conducted using various physical models. In the present study, a following large-eddy model, in which effects of large-scale turbulence can be considered, is used for our measured data.

$$k_+ S_c^{1/2} \propto R_e^{-1/2} \tag{6}$$

in which, $k_+ \equiv kU_m / u'_c$ is transfer velocity normalized by velocity-scales. u'_c is space-averaged turbulence intensity along the boundary between the main-channel and the side-cavity. $Re \equiv u'_c L_p / \nu$ is Reynolds number. L_p is the length scale of PG. Sc is Schmidt number and Sc is chosen as 1. Fig.15 shows relation between the normalized transfer velocity and Reynolds number. It is found that the present data coincide well with the large-eddy model. So, it is suggested that when the length scale of PG and turbulent intensity are accuraltely given, transfer velocity could be predicted reasonably, irrespective of bed configrations.

5. Conclusion

In this chapter, the open-channel flows with dead water zone were highlighted, and the effects of sedimentation on horizontal circulation structure and related mass-exchanges were considered on the basis of the measured data obtained by the laboratory experiments.

The both of MG and SG are observed in the flat-bed and downward slope conditions, and in contrast, the only MG appears in the upward slope condition. It was found that these formations of the horizontal circulations play significant roles on the mass transfer properties between the mainstream and the cavity. So, we should consider the effects of the bed configuration, when the turbulence structure and the related mass transfer phenomena are evaluated in detail.

6. References

Akkerman, G.J., van Heereveld, M.A., van der Wal, M. & Stam, J.M.T.(2004). Groyne optimization and river hydrodynamics, *Proc. Riverflow* 2004, Napoli, on CD-ROM.

Borg,A., Bolinger,J. & Fuchs,L.(2001). Simultaneous velocity and concentration measurements in the near field of a turbulent low-pressure jet by digital particle image velocimetry-planar laser-induced fluorescence, *Exp fluids* 31, 140-152.

Chong, M.S. & Perry, A.E. (1990). A general classification of three-dimensional flow fields. *Phys. Fluids* A, 2, 765-777.

Kadota, A. & Suzuki, K. (2010). Local scour and development of sand wave around a permeable groyne of stone gabion, *Environmental Hydraulics*, *Christodoulou & Stamou (eds.)*, 807-812.

Tominaga, A. & Sakaki, T. (2010). Evaluation of bed shear stress from velocity measurements in gravel-bed river with local non-uniformity, *Riverflow 2010*, *Dittrich, Koll, Aberle & Geisenhainer (eds)*, 187-194.

Uijttewaal, W.S.J., D. Lehmann & van Mazijk, A. (2001). Exchange processes between a river and its groyne fields: Model experiments, *Journal of Hydraulic Engineering*, ASCE, 1273(11), 928-936.

Weitbrecht, V., Socolofsky,S.A. & Jirka, G.H. (2007). Experiments on mass exchage between groin fields and main stream in rivers, *Journal of Hydraulic Engineering*, ASCE, 134(2), 173-183.
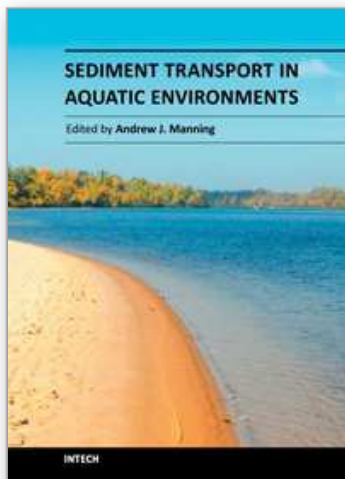
Sediment Transport in Aquatic Environments

Edited by Dr. Andrew Manning

Sediment Transport in Aquatic Environments is a book which covers a wide range of topics. The effective management of many aquatic environments, requires a detailed understanding of sediment dynamics. This has both environmental and economic implications, especially where there is any anthropogenic involvement. Numerical models are often the tool used for predicting the transport and fate of sediment movement in these situations, as they can estimate the various spatial and temporal fluxes. However, the physical sedimentary processes can vary quite considerably depending upon whether the local sediments are fully cohesive, non-cohesive, or a mixture of both types. For this reason for more than half a century, scientists, engineers, hydrologists and mathematicians have all been continuing to conduct research into the many aspects which influence sediment transport. These issues range from processes such as erosion and deposition to how sediment process observations can be applied in sediment transport modeling frameworks. This book reports the findings from recent research in applied sediment transport which has been conducted in a wide range of aquatic environments. The research was carried out by researchers who specialize in the transport of sediments and related issues. I highly recommend this textbook to both scientists and engineers who deal with sediment transport issues.

How to reference

In order to correctly reference this scholarly work, feel free to copy and paste the following:

Michio Sanjou (2011). Hydrodynamic Effects of Sedimentation on Mass Transport Properties in Dead Water Zone of Natural Rivers, Sediment Transport in Aquatic Environments, Dr. Andrew Manning (Ed.), ISBN: 978-953-307-586-0, InTech, Available from: http://www.intechopen.com/books/sediment-transport-in-aquatic-environments/hydrodynamic-effects-of-sedimentation-on-mass-transport-properties-in-dead-water-zone-of-natural-riv

INTECH
open science | open minds